

An Approach for Observing and Modeling Errors in MEMS-Based Inertial Sensors Under Vehicle Dynamic

Yannick Stebler, Stéphane Guerrier, and Jan Skaloud

Abstract—This paper studies the error behavior of low-cost inertial sensors in dynamic conditions. After proposing a method for error observations per sensor (i.e., gyroscope or accelerometer) and axes, their properties are estimated via the methodology of generalized method of wavelet moments. The developed model parameters are compared with those obtained under static conditions. Then, an attempt is presented to link the parameters of the established model to the dynamic of the vehicle. It is found that a linear relation explains a large portion of the exhibited variability. These findings suggest that the static methods employed for the calibration of inertial sensors could be improved when exploiting such a relationship.

Index Terms—Errors, estimation, inertial measurement unit (IMU), integration, modeling.

NOMENCLATURE

<i>b</i> -frame	Frame fixed to vehicle.
<i>c</i> -frame	Computer frame.
<i>i</i> -frame	Inertial space.
<i>l</i> -frame	True north–east–down frame.
<i>s</i> -frame	Frame fixed to sensor <i>s</i> .
DCM	Direction cosine matrix.
EKF	Extended Kalman filter.
GMWM	Generalized method of wavelet moments.
GNSS	Global navigation satellite system.
GPS	Global positioning system.
IMU	Inertial measurement unit.
INS	Inertial navigation system.
MEMS	Microelectromechanical system.
Rf-IMU	Reference IMU.
S-IMU	Studied IMU.
\mathbf{x}^y	Vector \mathbf{x} expressed in the <i>y</i> -frame.
$\dot{\mathbf{x}}$	Time derivative of \mathbf{x} .
ω_{xy}^z	Angular velocity of the <i>y</i> -frame with respect to the <i>x</i> -frame, resolved in the <i>z</i> -frame.

Manuscript received November 23, 2014; revised April 1, 2015; accepted April 2, 2015. Date of publication July 15, 2015; date of current version October 7, 2015. The Associate Editor coordinating the review process was Dr. Salvatore Baglio.

Y. Stebler and J. Skaloud are with the Geodetic Engineering Laboratory, École Polytechnique Fédérale de Lausanne, Lausanne 1015, Switzerland (e-mail: yannick.stebler@gmail.com; jan.skaloud@epfl.ch).

S. Guerrier is with the Department of Statistics, University of Illinois at Urbana–Champaign, Champaign, IL 61820 USA (e-mail: stephane@illinois.edu).

Digital Object Identifier 10.1109/TIM.2015.2444239

\mathbf{C}_x^y DCM representing the attitude of the *x*-frame with respect to the *y*-frame.

$[\mathbf{v} \times]$ Vector product. If $\mathbf{v} = [v_x \ v_y \ v_z]^T$, then

$$[\mathbf{v} \times] = \begin{bmatrix} 0 & -v_z & v_y \\ v_z & 0 & -v_x \\ -v_y & v_x & 0 \end{bmatrix}.$$

I. INTRODUCTION

The integration of a strapdown INS with satellite-based systems (GNSS) using Bayesian techniques, usually the EKF, is a standard approach for reliably estimating at any time the navigation states (i.e., position, velocity, and attitude in space) of a vehicle. The INS comprises an IMU formed by a triad of usually orthogonally mounted gyroscopes and accelerometers observing angular rate or change, and specific force, respectively. After initialization, these signals are integrated with respect to time to yield attitude, velocity, and finally, position. During periods of poor GNSS signal quality or when no GNSS solution can be computed by the receiver, inertial navigation (in the case of loosely coupled integration) operates in coasting mode, i.e., the navigation states are estimated independently from satellite data. In such a case, the overall navigation performance becomes strongly dependent on the errors corrupting inertial signals. These errors are integrated in the INS making their impact grow with time. Correct error modeling and estimation of their systematic part is thus essential for enhancing and correctly predicting its quality.

Inertial sensors are corrupted by errors (e.g., scale factors and biases) of deterministic and stochastic nature. A broad part of the systematic components (e.g., axis misalignments, temperature-dependent effects, and constant offsets) is compensated through physical models during in-lab calibration procedures [1], [2]. For instance, recommended procedures for MEMS gyros testing and calibration are described in [3]. The reference signals may also be dynamically provided within laboratory environment, for instance, through employment of single- or multiple-axis rotation tables [2], [4]. The cost of such equipment is very high and, as mentioned in [5] for the case of low-cost inertial sensors, the method may not provide optimal estimate of all calibration coefficients. The reason is that in the case of such sensors, the stochastic errors involve effects that are too complicated to model deterministically (e.g., residual effects due to

environmental changes and internal sensor noise) or have random behavior (e.g., vibrations). They are usually modeled by stochastic processes that drive augmented states accommodating for sensor biases in the EKF. The choice of the process and the estimation of their parameters is traditionally done using the *Allan variance* (AV) method [6], [7], or more recently, the GMWM framework introduced in [8] (see also [9], [10]).

A kinematic calibration usually follows static calibration, and examples of in-flight calibration can be found in [11] and [12]. However, the reference rate may not be readily available and needs to be estimated. Reference [13] claims that GPS/INS field testing is the only way to evaluate the performance of MEMS IMUs in a realistic situation, but the procedure is rather complicated. The same reference proposes a cost-effective emulation approach that can be summarized in four steps: 1) collecting long-term static signals; 2) conducting a field test together with a reference IMU; 3) emulating the statically observed error signals on reference IMU; and 4) integrating the emulated data with GNSS and evaluating the results. Naturally, conducting emulations with dynamically observed errors are likely to provide more realistic scenario for IMU evaluation; however, the construction of error models using the previously mentioned calibration procedures does not necessarily consider the platform dynamics. The reason is that the error signals are constructed from the variations of sensor's output, while its input is assumed to be constant. In other words, these models may correspond well to the observed variations, but not for their possible modifications caused by the motion. Effects like vibrations or scale-dependent errors may further affect the error characteristics. To the best of the authors' knowledge, the published attempts that construct and characterize the dynamically dependent error processes in the observation domain of low-cost inertial sensors are rare. Some preliminary results were obtained in [14] and [15] in which dynamics-dependent error behavior affecting a tactical-grade and low-cost IMU was highlighted.

The goal of this paper is hence twofold.

- 1) We describe how error signals can be properly constructed in dynamic conditions per sensor axis using a reference IMU of navigation-grade quality. Although simple in its formulation, the spatial, rotational, sampling frequency, and time-alignment issues make this task clearly nontrivial, which perhaps explain the absence of detailed literature on this subject.
- 2) We study the nature of the relationship between the sensor errors and the platform dynamics, and propose a suitable strategy for data processing.

The rest of this paper is organized as follows. We first show in Section II how error signals can be properly constructed from sensors operating on a car. Once these signals are available, we investigate MEMS-based error signals in Sections III and IV before moving to propositions for dealing with dynamic dependency in navigation filters in Section VII. Finally, Section VIII provides general conclusions and perspectives.

II. ERROR SIGNAL CONSTRUCTION

The sensor error signal generation requires the less straightforward definition and calibration of the following relationships: the spatial and rotational offsets between the triads forming the IMUs and the time alignment of both devices to a common reference. Once the data have been space and time aligned, the sensor error is simply the difference between the transformed sensor signals delivered by the S-IMU and the reference signals. This section develops two methods allowing for spatial alignment between the reference and the S-IMU sensor signals.

Consider the Rf-IMU and the S-IMU rigidly mounted on the same platform. Assume that the b -frame is equivalent to the Rf-IMU instrumental frame and that the S-IMU provides observations in his instrumental s -frame. The b -frame and s -frame origins are separated by a vector $\mathbf{r}_{b \rightarrow s}^b$, called *inter-IMU lever arm*, and their relative orientation is expressed by the \mathbf{C}_b^s direction cosine matrix, called *inter-IMU boresight*. The relationship between \mathbf{C}_b^s and the estimated boresight, denoted as $\hat{\mathbf{C}}_b^s$, may be expressed in terms of misalignment errors as

$$\mathbf{C}_b^s = (\mathbf{I} + \boldsymbol{\Psi}) \hat{\mathbf{C}}_b^s \quad (1)$$

where $\boldsymbol{\Psi} = [\psi_{b \rightarrow s}^b \times]$ is a skew-symmetric matrix containing the misalignment error angles $\psi_{b \rightarrow s}^b = [\psi_x \ \psi_y \ \psi_z]^T$ between the b -frame and the s -frame. The (3×1) observed S-IMU angular rate ω_{is}^s (which is equivalent to ω_{ib}^s on a rigid body) and specific force \mathbf{f}^s vectors must be corrected by boresight \mathbf{C}_b^s and lever-arm $\mathbf{r}_{b \rightarrow s}^b$ effects, respectively. Both quantities can either be known *a priori* or estimated by means of an EKF whose states are defined as

$$\mathbf{x} = [\delta \mathbf{r}_e^l \ \delta \mathbf{v}_e^l \ \boldsymbol{\epsilon}^l \ \delta \mathbf{f}^b \ \delta \omega_{ib}^b \ \delta \mathbf{x}_c]^T \quad (2)$$

with $\delta \mathbf{r}_e^l = [\delta \phi \ \delta \lambda \ \delta h]^T$ the errors in latitude ϕ , longitude λ , and height h , $\delta \mathbf{v}_e^l = [\delta v_N \ \delta v_E \ \delta v_D]^T$ the errors in north, east, and down (NED) velocity components, and the misalignment angles $\boldsymbol{\epsilon}^l = [\varepsilon_N \ \varepsilon_E \ \varepsilon_D]^T$ expressing the attitude errors with respect to the NED l -frame. The $\delta \mathbf{f}^b$ and $\delta \omega_{ib}^b$ are vectors of size (3×1) each accounting for accelerometer and gyroscope biases, respectively. The $\delta \mathbf{x}_c$ vector contains inter-IMU calibration states, e.g., $[\psi_{b \rightarrow s}^b, \mathbf{r}_{b \rightarrow s}^b]$, the modeling and observation of which is treated in the next two sections.

The linearized position error model is

$$\delta \dot{\mathbf{r}}_e^l = -\boldsymbol{\omega}_{el}^l \times \mathbf{r}_e^l + \delta \boldsymbol{\theta} \times \mathbf{v}_e^l + \delta \mathbf{v}_e^l \quad (3)$$

with $\delta \boldsymbol{\theta}$ the misalignment vector of computer c -frame [16] with respect to l -frame as a consequence of position error

$$\delta \boldsymbol{\theta} = [\delta \lambda \cos \phi \ -\delta \phi \ -\delta \lambda \sin \phi]^T. \quad (4)$$

The velocity error model is

$$\begin{aligned} \delta \dot{\mathbf{v}}_e^l &= -\mathbf{f}^l \times \boldsymbol{\epsilon}^l - (\boldsymbol{\omega}_{ie}^l + \boldsymbol{\omega}_{il}^l) \times \delta \mathbf{v}_e^l \\ &\quad - (\delta \boldsymbol{\omega}_{ie}^l + \delta \boldsymbol{\omega}_{il}^l) \times \mathbf{v}_e^l + \mathbf{C}_b^l \delta \mathbf{f}^b + \delta \mathbf{g}^l. \end{aligned}$$

The attitude error model is

$$\dot{\boldsymbol{\epsilon}}^l = -\boldsymbol{\omega}_{il}^l \times \boldsymbol{\epsilon}^l + \delta \boldsymbol{\omega}_{il}^l - \mathbf{C}_b^l \delta \boldsymbol{\omega}_{ib}^b. \quad (5)$$

The establishment of sensor models is the goal of this paper and will be discussed in Section IV. Furthermore, as it is assumed that S-IMU is rigidly mounted to the same platform as the Rf-IMU, the transformation parameters from one IMU to the other are constant in time

$$\delta \dot{\mathbf{x}}_c = 0. \quad (6)$$

In the sequel, two methods based on the described EKF are developed.

A. Boresight Estimation Through Attitude Update

This method, also used in [17], estimates \mathbf{C}_b^s in the S-IMU/GNSS EKF by employing attitude updates issued from the Rf-IMU/GNSS processed solution. The S-IMU/GNSS filter can be fed with \mathbf{z}_φ measurements issued from the Rf-IMU/GNSS filter state

$$\mathbf{z}_\varphi = [z_r \ z_p \ z_y]^T$$

where z_r , z_p , and z_y are roll, pitch, and yaw observations, respectively. If again the same assumption of small ψ_x , ψ_y , and ψ_z angles is made, the measurement model can be expressed as

$$\mathbf{z}_\varphi = h(\mathbf{x}_c) + \mathbf{v}_\varphi \approx (\mathbf{I} - \boldsymbol{\Psi})\varphi + \mathbf{v}_\varphi \quad (7)$$

where $\mathbf{x}_c(1 : 3) = \psi_{b \rightarrow s}^b$ are the augmented states and $\varphi = [r \ p \ y]^T$ is the vector containing the attitude angles estimated in the S-IMU/GNSS EKF.¹ Linearizing the model expressed in (7) yields the following observation design matrix:

$$\mathbf{H}_\varphi = [\mathbf{0}_{3 \times 6} | (\mathbf{I}_{3 \times 3} - \boldsymbol{\Psi}) | \mathbf{0}_{3 \times 6} | [\boldsymbol{\epsilon}^l \times]].$$

This method works well for systems based on higher grade sensors. However, if the S-IMU is of poor quality, the solution provided by the S-IMU/GNSS filter may be considerably affected by the imperfections of the initialization stage. Therefore, working with the Rf-IMU/GNSS filter as described further may be advantageous.

B. Joint Boresight and Lever-Arm Estimation Through Specific Force and Angular Rate Update

This method enables joint \mathbf{C}_b^s and $\mathbf{r}_{b \rightarrow s}^b$ estimation by feeding the Rf-IMU/GNSS filter with the less precise ω_{is}^s and \mathbf{f}^s measurements. The relation between ω_{is}^s and ω_{ib}^b is given by

$$\omega_{is}^s = \mathbf{C}_b^s \omega_{ib}^b \quad (8)$$

which is true under the conditions that $\dot{\mathbf{C}}_b^s = 0$ and $\dot{\mathbf{r}}_{b \rightarrow s}^b = 0$. If $\Omega_{is}^s = [\omega_{is}^s \times]$ and $\Omega_{ib}^b = [\omega_{ib}^b \times]$, the relation between \mathbf{f}^b and \mathbf{f}^s can be written as [18]

$$\mathbf{f}^s = \mathbf{C}_b^s (\mathbf{f}^b + \dot{\Omega}_{ib}^b \mathbf{r}_{b \rightarrow s}^b + \Omega_{ib}^b \Omega_{ib}^b \mathbf{r}_{b \rightarrow s}^b) \quad (9)$$

in which $\dot{\Omega}_{ib}^b \mathbf{r}_{b \rightarrow s}^b$ and $\Omega_{ib}^b \Omega_{ib}^b \mathbf{r}_{b \rightarrow s}^b$ represent the tangential and centrifugal forces, respectively.

Under the condition that ψ_x , ψ_y , and ψ_z are small, we have $\mathbf{C}_b^s \approx \mathbf{I} - \boldsymbol{\Psi}$. By denoting ω_{is}^s and \mathbf{f}^s , respectively, as \mathbf{z}_ω and \mathbf{z}_f , the measurement models given in (8) and (9) are

$$\mathbf{z}_\omega = h(\mathbf{x}_c) + \mathbf{v}_\omega \approx \Omega_{ib}^b \psi_{b \rightarrow s}^b + \mathbf{v}_\omega \quad (10)$$

¹These values are obtained from \mathbf{C}_b^l for S-IMU.

and

$$\begin{aligned} \mathbf{z}_f &= h(\mathbf{x}_c) + \mathbf{v}_f \\ &\approx -([\mathbf{f}^b \times] + \Omega_{ib}^b \Omega_{ib}^b [\mathbf{r}_{b \rightarrow s}^b \times] + \dot{\Omega}_{ib}^b [\mathbf{r}_{b \rightarrow s}^b \times]) \psi_{b \rightarrow s}^b \\ &\quad + \mathbf{C}_b^s (\Omega_{ib}^b \Omega_{ib}^b + \dot{\Omega}_{ib}^b) \delta \mathbf{r}_{b \rightarrow s}^b + \mathbf{v}_f \end{aligned} \quad (11)$$

where

$$\mathbf{x}_c = [(\psi_{b \rightarrow s}^b)^T \ (\mathbf{r}_{b \rightarrow s}^b)^T]^T$$

are the augmented calibration states. The design matrix \mathbf{H}_f for the whole state vector can be deduced from (10) and (11), yielding

$$\mathbf{H}_f = \left[\begin{array}{c|c} \mathbf{0}_{3 \times 15} & \mathbf{0}_{3 \times 15} \\ \Omega_{ib}^b & -[\mathbf{f}^b \times] - \Omega_{ib}^b \Omega_{ib}^b [\mathbf{r}_{b \rightarrow s}^b \times] - \dot{\Omega}_{ib}^b [\mathbf{r}_{b \rightarrow s}^b \times] \\ \mathbf{0}_{3 \times 3} & \mathbf{C}_b^s (\Omega_{ib}^b \Omega_{ib}^b + \dot{\Omega}_{ib}^b) \end{array} \right]^T. \quad (12)$$

Note that the estimation of \mathbf{C}_b^s using this method presents several advantages compared with Section II-A.

- 1) The Rf-IMU/GNSS EKF is based on a navigation-grade IMU whose gyroscope and accelerometer error models are well known. This enables a much more precise initialization (especially the coarse alignment) and less drift during periods where the car was stopped (at red lights or crossroads). Note that the EKF implemented zero-velocity updates (ZUPT) during these periods.
- 2) The Rf-IMU/GNSS EKF IMU materializes the b -frame implying no dependency between $\boldsymbol{\epsilon}^l$ and $\psi_{b \rightarrow s_i}^b$ as shown in (12). As $\boldsymbol{\epsilon}^l$ has a large initial uncertainty for MEMS-IMUs, this is especially important for data sets with poor dynamics on some directions (as is the case with cars) or of limited duration because $\boldsymbol{\epsilon}^l$ will have weakly observable components.

To verify the validity of the proposed algorithm, we emulated a low-grade (i.e., an S-IMU) and a tactical-grade IMU (i.e., an Rf-IMU) along a reference trajectory experienced by a car. The two emulated units were separated by a distance $\mathbf{r}_{b \rightarrow s}^b$ and misaligned by \mathbf{C}_b^s . In Fig. 1, we show the boresight angles extracted from $\hat{\mathbf{C}}_b^s$ and lever arm $\hat{\mathbf{r}}_{b \rightarrow s}^b$ estimated by means of the Rf-IMU/GNSS filter fed by the low-grade inertial measurements (forward filtering solution). The true boresight parameters $\mathbf{r}_{b \rightarrow s}^b$ and \mathbf{C}_b^s are depicted as thick gray lines. The augmented states $\psi_{b \rightarrow s}^b$ and $\mathbf{r}_{b \rightarrow s}^b$ were driven by the following Gauss-Markov processes:

$$\begin{aligned} \dot{\psi}_{b \rightarrow s}^b &= \beta_\psi \psi_{b \rightarrow s}^b + \mathbf{w}_\psi \\ \dot{\mathbf{r}}_{b \rightarrow s}^b &= \beta_r \mathbf{r}_{b \rightarrow s}^b + \mathbf{w}_r \end{aligned}$$

where β_ψ and β_r are (3×1) vectors containing the inverse correlation times set to large values (i.e., are practically random constants), and $\mathbf{w}_\psi \sim \mathcal{N}(\mathbf{0}, \sigma_\psi^2)$ and $\mathbf{w}_r \sim \mathcal{N}(\mathbf{0}, \sigma_r^2)$ are driving noise with PSD levels σ_ψ^2 and σ_r^2 of the processes associated with the boresight and lever-arm states, respectively. The filter was initialized with null values for both boresight and lever-arm states. The convergence time to the true values lasts only a few seconds, with initial $\sigma_{\psi_{b \rightarrow s}} = 20$ [deg] and $\sigma_{r_{b \rightarrow s}} = 20$ [cm].

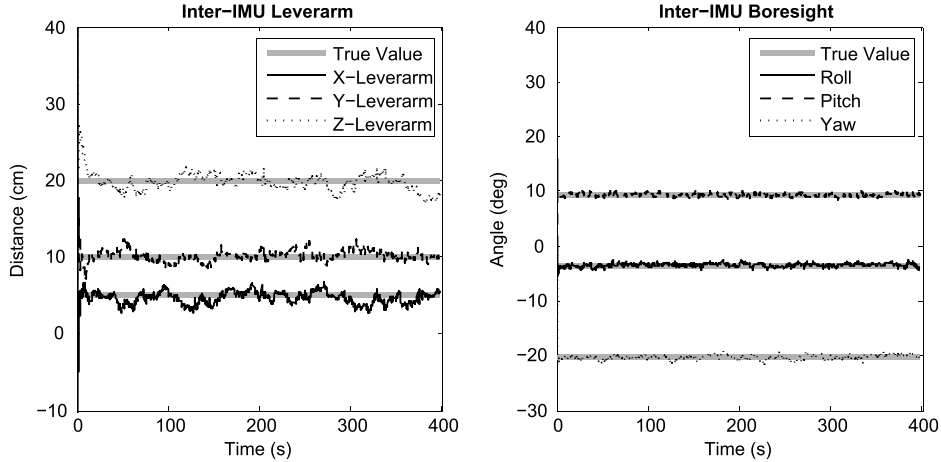


Fig. 1. Result of a joint inter-IMU lever-arm (left panel) and boresight (right panel) estimation using emulated IMUs. The true values are shown as gray lines.

III. ANALYSIS OF THE DEPENDENCY OF THE ERRORS OF MEMS-IMUs ON DYNAMICS

Similar to the analysis performed in [14], the dependency of the constructed error signals on some quantities representing the dynamics can be highlighted using descriptive statistics. Let the sequence of digital times be denoted by $\{t_k : k = 1, \dots, N\}$. The chosen quantities are the linear acceleration (i.e., the specific force from which the gravity component has been added using the attitude matrix C_b^l estimated by the navigation filter and the gravity model proposed in [19]) and linear jerk expressed in the b -frame, respectively, noted by the vectors

$$\mathbf{a}_k^b = \begin{bmatrix} a_{x,k} \\ a_{y,k} \\ a_{z,k} \end{bmatrix}, \quad \dot{\mathbf{a}}_k^b = \begin{bmatrix} \dot{a}_{x,k} \\ \dot{a}_{y,k} \\ \dot{a}_{z,k} \end{bmatrix}$$

and the angular velocity, angular acceleration, and angular jerk, respectively, noted by

$$(\boldsymbol{\omega}_{ib}^b)_k = \begin{bmatrix} \omega_{x,k} \\ \omega_{y,k} \\ \omega_{z,k} \end{bmatrix}, \quad (\dot{\boldsymbol{\omega}}_{ib}^b)_k = \begin{bmatrix} \dot{\omega}_{x,k} \\ \dot{\omega}_{y,k} \\ \dot{\omega}_{z,k} \end{bmatrix}$$

$$(\ddot{\boldsymbol{\omega}}_{ib}^b)_k = \begin{bmatrix} \ddot{\omega}_{x,k} \\ \ddot{\omega}_{y,k} \\ \ddot{\omega}_{z,k} \end{bmatrix}.$$

To verify the dependency between the errors of the sensors and some of the quantities representative for the dynamics, the following linear model can be constructed:

$$\begin{aligned} y_k = & \beta_1 \omega_{x,k} + \beta_2 \omega_{y,k} + \beta_3 \omega_{z,k} + \beta_4 \dot{\omega}_{x,k} \\ & + \beta_5 \dot{\omega}_{y,k} + \beta_6 \dot{\omega}_{z,k} + \beta_7 \ddot{\omega}_{x,k} + \beta_8 \ddot{\omega}_{y,k} \\ & + \beta_9 \ddot{\omega}_{z,k} + \beta_{10} a_{x,k} + \beta_{11} a_{y,k} + \beta_{12} a_{z,k} \\ & + \beta_{13} \dot{a}_{x,k} + \beta_{14} \dot{a}_{y,k} + \beta_{15} \dot{a}_{z,k} + \varepsilon_k \end{aligned} \quad (13)$$

with $k = 1, \dots, N$ and y_k can denote either the (dynamic) errors of a gyroscopes or an accelerometer on the x -, y -, or z -axis. It can be assumed that $\varepsilon \sim \mathcal{N}(0, \sigma_\varepsilon^2)$.

The β_j parameters can be obtained by fitting models (13) iteratively (starting from the full model) and removing at

each iteration least significant parameter until all parameters become significant at the 5% confidence level.

In addition, the coefficient of determination (i.e., R^2) and p -value associated with the F -test can be computed for each regression. In general terms, the R^2 is a statistic belonging to $[0, 1]$, which summarizes how much of the change in error can be explained by the dynamics (0 being no explanation and 1 being complete explanation). The F -test is an additional statistical inference procedure, which understands whether at least some of the dynamics explain the behavior in the error by testing the following hypotheses:

$$\begin{aligned} H_0 : \boldsymbol{\beta} &= \mathbf{0} \\ H_a : \boldsymbol{\beta} &\neq \mathbf{0} \end{aligned} \quad (14)$$

where $\boldsymbol{\beta} = [\beta_j]_{j=1, \dots, 15}$. The null hypothesis H_0 basically says that all 15 coefficients are null, meaning that none of the dynamics explain the error, while the alternative hypothesis H_a says that at least one of the dynamics explains the behavior of the error.

IV. ERROR STRUCTURE ANALYSIS THROUGH STOCHASTIC MODELING

The stochastic behavior of inertial sensors in static and dynamic conditions can be analyzed by means of the recently developed GMWM estimation framework, which is briefly introduced in this section.

The GMWM estimator was first proposed in [8] in which several important properties such as its consistency and its asymptotic normality were demonstrated. In [20], this estimation method was successfully applied for calibrating inertial sensors using more sophisticated stochastic processes and, thus, improving EKF navigation performance. Guerrier *et al.* [8] demonstrated that the method of AV [6]² leads in general to inconsistent estimators and that there exists always a GMWM estimator with smaller asymptotic variance than its AV-based counterpart. The simulation studies presented in [8] and [10] also illustrate that the GMWM is able to estimate models for which classical methods such as the AV or likelihood-based estimators fail.

²A recommended standard of Institute of Electrical and Electronics Engineers since 1997 (IEEE Std 952-1997).

Consider the sequence $\{y_k : k = 1, \dots, N\}$ representing the observed 1-D noncompensated error signal of an accelerometer or a gyroscope. This sequence is assumed to be a realization of an univariate Gaussian stochastic process $\{Y_k : k \in \mathbb{Z}\}$ that is stationary or nonstationary but with backward difference³ of order d and associated with the model F_θ with parameters $\theta \in \Theta \subseteq \mathbb{R}^p$.

The GMWM exploits the link that exists between F_θ and *wavelet variances* (WVs) through the mapping

$$\theta \mapsto v(\theta) \quad \forall \theta \in \Theta$$

where $v(\theta) = [v_j(\theta)]_{j=1,\dots,J}$, $J \in \{x \in \mathbb{N}^+ | 1 < x \leq \log_2(T), x < \infty\}$, and we have that

$$v_j(\theta) = \int_{-1/2}^{1/2} |\tilde{H}_j(f)|^2 S_{F_\theta}(f) df \quad (15)$$

in which $\tilde{H}_j(f)$ is the transfer function of the j th wavelet filter $\tilde{h}_{j,l}$ and $S_{F_\theta}(f)$ is the PSD of the signal generated by model F_θ . By combining the above mapping with the principle of least squares, one can define a suitable estimator of θ . Indeed, the GMWM estimators aim to inverse (in some sense) the above mapping by trying to approximate the point $\theta(\hat{v})$, where \hat{v} denotes a suitable estimator of the WV computed on the observed outcome $\{y_t\}$. In other words, the GMWM aims to find the value of θ implied by \hat{v} . For that, the distance between \hat{v} and $v(\theta)$ has to be minimized. Therefore, GMWM estimators are defined as the solution to the following optimization problem:

$$\hat{\theta} = \underset{\theta \in \Theta}{\operatorname{argmin}} (\hat{v} - v(\theta))^T \Omega (\hat{v} - v(\theta)) \quad (16)$$

in which Ω , a positive definite weighting matrix,⁴ is chosen in a suitable manner [8]. The vectors $\hat{v} = [\hat{v}_j]_{j=1,\dots,J}$ and $v(\theta) = [v_j(\theta)]_{j=1,\dots,J}$ represent, respectively, the maximal overlap discrete wavelet transform estimator of the WV and the WV implied by model for the parameter vector θ . Thus, the solution to (16) corresponds to the point, where $v(\theta)$ is the closest possible approximation of \hat{v} with respect to the weighting matrix Ω .

A common choice of the matrix Ω is V_{diag}^{-1} , where the elements of V_{diag} are given by

$$(V_{\text{diag}})_{i,j} = \begin{cases} \widehat{\text{var}}(\hat{v}_i), & \text{if } i = j \\ 0, & \text{if } i \neq j \end{cases} \quad (17)$$

where $\widehat{\text{var}}(\hat{v}_i)$ is a suitable estimator of the variance of \hat{v}_i (see [21] for more details). Note that for the WV based on Haar wavelet filters and for the processes that will be considered in this paper, the integral in (15) can be solved explicitly (see [8] for their expressions that are obtain based on the results of [22]). When analytical expressions are not available for $v(\theta)$, this quantity can be approximated by simulations, thus placing the GMWM in the framework of indirect estimation proposed in [23]. Reference [8, Corollary 3] demonstrates that this estimation

³The first-order backward difference of Y_t is $Y_t^{(1)} = Y_t - Y_{t-1}$ and the backward difference of order d is $Y_t^{(d)} = Y_t^{(d-1)} - Y_{t-1}^{(d-1)}$.

⁴ Ω has to be positive definite in order to ensure the convexity of (16).

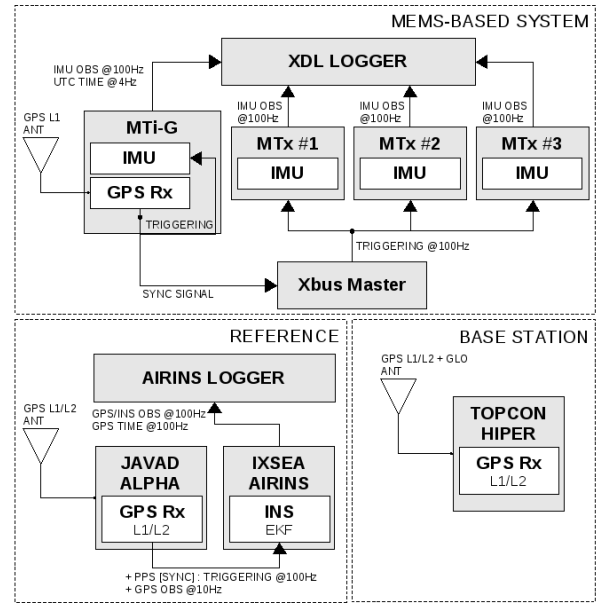


Fig. 2. Instrumental setup used for error signal generation in dynamic conditions.

technique is consistent and asymptotically distributed for all the models commonly used to model inertial sensors, and therefore this enables to compute (asymptotic) confidence intervals on the estimated parameters $\hat{\theta}$.

V. EXPERIMENT

An acquisition campaign was conducted for generating error signals with respect to an Rf-IMU operated on the same platform as some S-IMUs.

A. Hardware

The experimental setup (Fig. 2) is composed of two subsystems.

- 1) The *MEMS-based system* composed of three XSens MTx MEMS-based S-IMUs and one XSens MTi-G⁵ unit (also containing a GPS receiver) sampled and logged simultaneously at 100 Hz.
- 2) The *reference system* comprising an Ixsea Airins⁶ navigation-grade INS (Rf-IMU) logging at 100 Hz combined with a geodetic-grade Javad's TR-G2T OEM board in Alpha enclosure L1/L2 GPS rover receiver (sampling at 10 Hz), and a Topcon Hiper Pro L1/L2 GPS base receiver (sampling at 5 Hz), both used for computing a double-differenced carrier-phase GPS solution.

All data were logged and GPS time referenced in real time by dedicated software (*Airins Logger*). The reference data were postprocessed through Kalman filtering and smoothing yielding compensated inertial signals.

B. Space and Time Alignment

Spatial alignment was achieved by applying the methodology developed in Section II-B on the S-IMU

⁵XSens MTx/MTi-G: noise $\approx 0.05 \text{ deg/s}/\sqrt{\text{Hz}}$, drift $\approx 1 \text{ deg/s}$.

⁶IxBLUE Airins: gyro-noise $< 0.0015 \text{ deg}/\sqrt{\text{Hz}}$, gyro-drift $< 0.01 \text{ deg/Hr}$, accel-bias $< 100 \mu\text{g}$, and accel-noise $< 20 \mu\text{g}$.

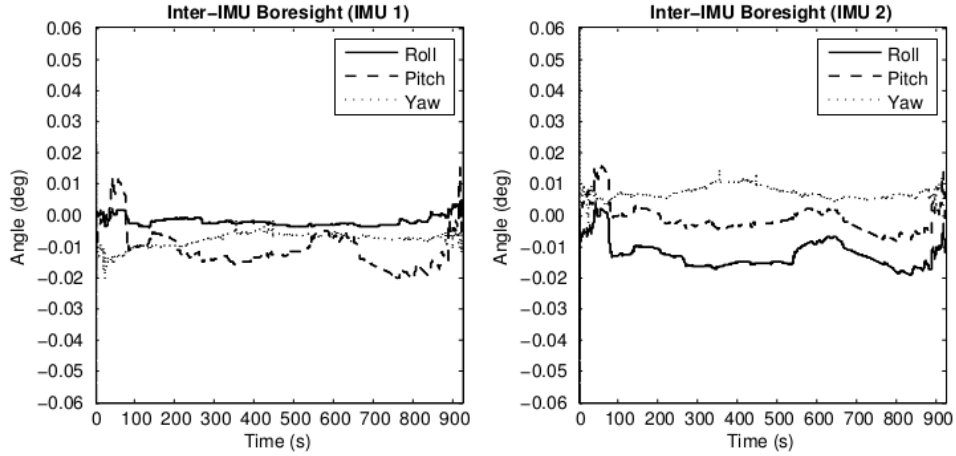


Fig. 3. Result of the inter-IMU boresight angle estimation for two *XSens MTx* IMUs using inertial measurements from an *Airins* navigation-grade IMU.

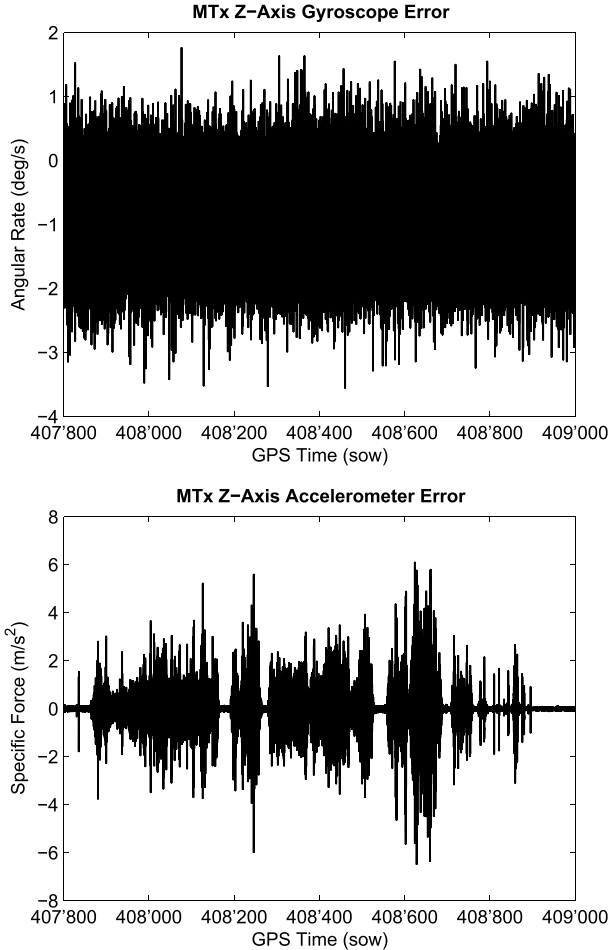


Fig. 4. Typical *XSens MTx* gyroscope (top panel) and accelerometer (bottom panel) error signals computed from the reference IMU under dynamics.

signals. Fig. 3 shows the estimated smoothed inter-IMU angles $\hat{\psi}_{b \rightarrow s_i}^b$ with $i = 1$ and 2 for two of the *XSens MTx* S-IMUs (measuring in their respective s_i instrumental frame) with respect to the reference signals provided by the *Airins* Rf-IMU. The data were collected on a vehicle during a 15-min-long trajectory. The final boresight angles are estimated as a weighted mean (considering the smoothed variances).

Besides the spatial alignment, the Rf-IMU and S-IMU data need to be aligned with respect to time. The GPS receiver contained in the *MTi-G* device yields access to a globally available timing and synchronization framework, the GPS time. An experimental setup was built such that all individual *MTx* IMUs sample simultaneously in time (Fig. 2). With this respect, a periodic TTL pulse [1 Pulse Per Second (PPS)] delivered by the GPS receiver serves as the base for the measurements (Fig. 2). This pulse is aligned to GPS time. The PPS signal is brought as input to the *XBus master* as a scale that aligns the triggering of all *MTx* S-IMUs. The absolute timing of the IMU messages is performed by a specially developed real-time C++ based datalogger (the *XDL logger* in Fig. 2), which exploits available GPS time messages and the guaranteed (by hardware) synchronous triggering of *MTx* internal sensors. The resulting time registration of the S-IMU samples was achieved with an acceptable precision (estimated below 1 ms). The *Airins* samples are also registered with respect to GPS time by exploiting a PPS signal coming from the external GNSS receiver. Note that the differences between the *Airins* internal sampling times and the *MTi-G/MTx* internal sampling times are neglected (as well as sampling jitter in the *MTi-G/MTx* devices).

The error of the z -axis gyroscope and accelerometer over the complete run is depicted as a representative example in Fig. 4.

VI. RESULTS

A. Dependency of the Errors on Dynamics

Fig. 5 shows a scatter plot between the angular velocity, acceleration and jerk (Section III), and the gyroscope error signals obtained from the previously described experiments. It is clear that there seems to be some kind of dependency between the errors of the sensors and some of the quantities representative for the dynamics.

This statement is confirmed by Tables II and III, which present the estimated values for the parameters β_j , $j = 1, \dots, 15$ together with the R^2 statistics for, respectively, the errors of the gyroscopes and the accelerometers on the x -, y -, or z -axis. It can be observed

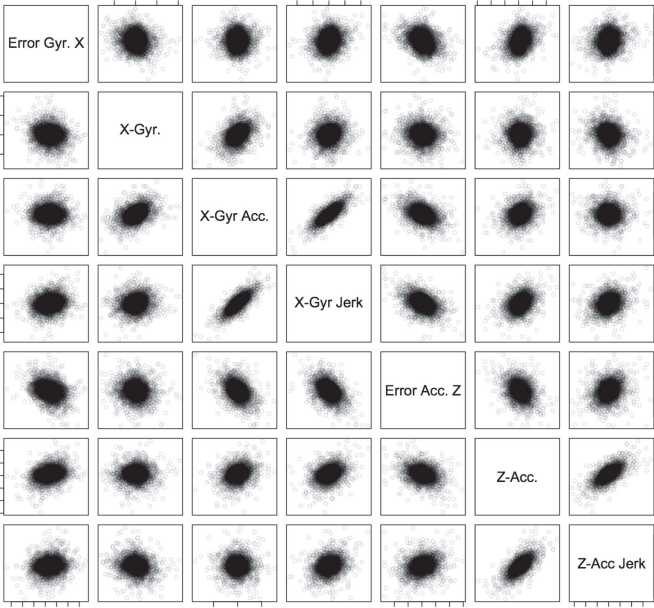


Fig. 5. Scatter plot between the errors of the gyroscope on the x axis, the angular velocity, the acceleration and jerk on the same axis, the errors of the accelerometer on the z axis, and the linear acceleration and linear jerk for the same axis.

that the H_α hypothesis formulated in Section III is considered as a valid hypothesis for all three axes taken into account in this analysis. Moreover, apart for the error coming from the z -axis of the gyroscope, the R^2 statistic tells us that a considerable amount of the error is explained by the dynamics. This clearly demonstrates that the dynamics has a statistically significant influence on the errors of the considered S-IMU.

B. Study of MEMS-Based Gyroscope and Accelerometer Stochastic Modeling

1) *Gyroscopes*: In the top panel of Fig. 6, we compare a typical (Haar) wavelet deviation⁷ sequence computed on the gyroscope error signal acquired in dynamic conditions (gray line with triangles) with its counterpart signal acquired in static conditions (black circles). These sequences are representative of the noise structure and can simply be observed as a rescaled version of the Allan deviation. A first look on the graph reveals that the noise structure may remain similar between nonmoving and moving conditions. However, this is not the case for the noise levels. To verify this statement formally, we fit a stochastic model on both the sequences corresponding to the static and dynamic conditions. We choose to model each error signal $\{y_k\}$ using a Gaussian white noise process mixed with a sum of $M (\in \mathbb{N})$ first-order Gauss–Markov processes to account for the correlated part of the errors. Such a model $F(\theta)$ can be written as

$$Y_k = \sum_{m=1}^M (Y_{GM,m})_k + W_k, \quad k \in \mathbb{R} \quad (18)$$

⁷The Allan/wavelet deviation is the root Allan/WV.

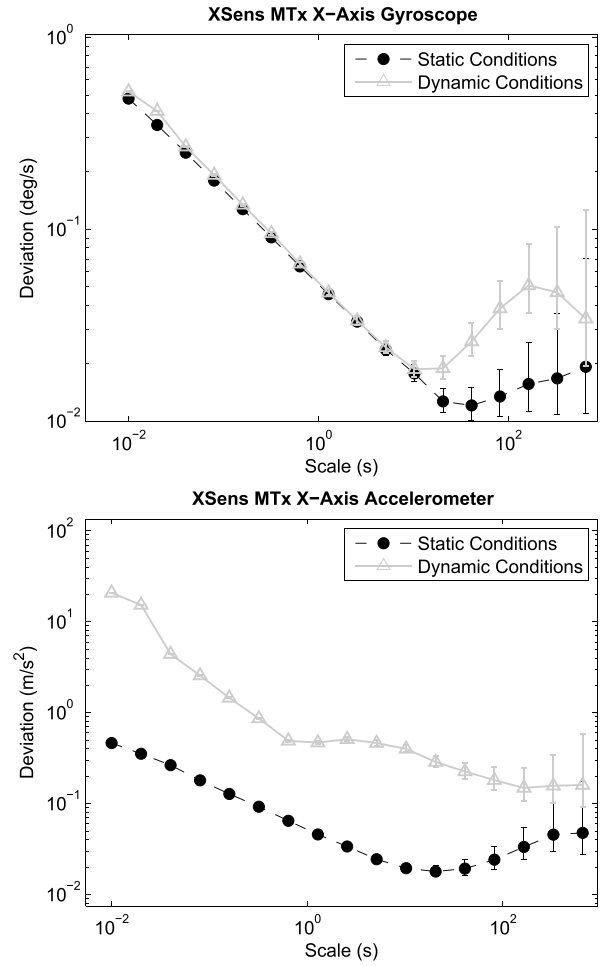


Fig. 6. Typical WV sequence computed on the gyroscope (top panel) and accelerometer (bottom panel) error signals acquired in moving conditions (black circles), together with the WV issued from an estimated model.

where $W_k \sim \mathcal{N}(0, \sigma_{WN}^2)$, and $(Y_{GM,m})_k$ is a discrete first-order Gauss–Markov process written by

$$(Y_{GM,m})_k = e^{-\beta \Delta t} (Y_{GM,m})_{k-1} + (W_{GM})_k$$

with $(W_{GM,m})_k \sim \mathcal{N}(0, \sigma_m^2)$ and $\sigma_m^2 = \sigma_{GM,m}^2 (1 - e^{-2\beta \Delta t})$. The set of parameters belonging to model (18) are therefore given by

$$\theta = \{\beta_m, \sigma_{GM,m}^2, \sigma_{WN}^2\}_{m=1,\dots,M}. \quad (19)$$

The choice of such a model is motivated by the fact that combinations of multiple Gauss–Markov processes can approximate many random processes [24]–[26].

After testing several values for M using the GMWM estimator, the best results (in terms of goodness of fit) for all gyroscope error signals (i.e., all axes) for nonmoving conditions were obtained with $M = 2$. Typical parameter values together with their corresponding 95% confidence intervals are listed in Table I in the *static model* column. We now build a model on the dynamic error signal using the same methodology with the intention of comparing the structure of the noise and its level with the static model. As a representative example, the result of the

TABLE I
COMPARISON BETWEEN THE XSens MTx GYROSCOPE MODEL CONSTRUCTED ON A SIGNAL ACQUIRED IN NONMOVING CONDITIONS (STATIC MODEL) AND IN MOVING CONDITIONS (DYNAMIC MODEL)

Process	Parameter	Unit	Static Model	Dynamic Model
Gaussian White Noise	σ_{WN}^2	(deg/s) ²	0.50552 ± 0.00035	0.65382 ± 0.00001
First-order Gauss-Markov #1	β_1	1/s	0.00492 ± 0.01892	0.00155 ± 0.00082
	$\sigma_{GM,1}^2$	(deg/s) ²	0.00142 ± 0.00001	0.00981 ± 0.00005
First-order Gauss-Markov #2	β_2	1/s	113.51523 ± 0.00404	1.68012 ± 0.04980
	$\sigma_{GM,2}^2$	(deg/s) ²	0.05528 ± 0.00051	0.00168 ± 0.00005

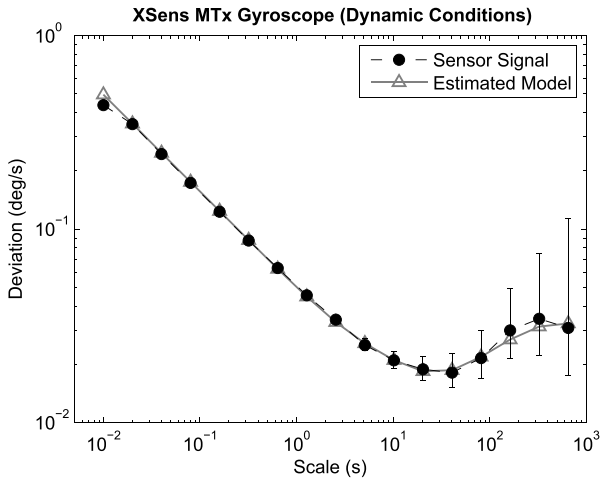


Fig. 7. WV sequence computed on the gyroscope error signal acquired in moving conditions (black circles), together with the WV issued from an estimated model.

GMWM-based modeling of the y -axis gyroscope dynamic error signal is shown in Fig. 7 in which we draw the wavelet deviation curve of the error signal (dashed black line with black circles) and the wavelet deviation of the estimated model (gray curve) $F(\hat{\theta})$. Again, after trying several values of M , the best results (in terms of goodness of fit) were obtained with $M = 2$. In Table I, we show the values of the estimated model parameters and the associated confidence intervals for the model constructed in dynamic conditions in the *dynamic model* column. Comparing both columns indicates that dynamics has not changed the gyroscope noise structure, i.e., that the navigation EKF can run with the same error model, independently from the vehicle dynamics. However, the magnitude of the Gaussian white noise level as well as the Gauss–Markov driving noise level and inverse correlation times differ since their confidence intervals do not overlap. A suggestion how to practically consider this in the navigation filter is given in Section VII.

2) *Accelerometers*: The same methodology as for the gyroscopes was applied on the accelerometers. In the bottom panel of Fig. 6, we show a typical wavelet deviation sequence computed on the error signals acquired in static (black circles) and dynamic (gray triangles) conditions. However, as it can already be concluded from Fig. 4, the accelerometers are clearly corrupted by vibrations,⁸ which make the

⁸This may be due to the fact that the sampling frequency of the accelerometers is not sufficiently high with respect to the frequency of vibrations.

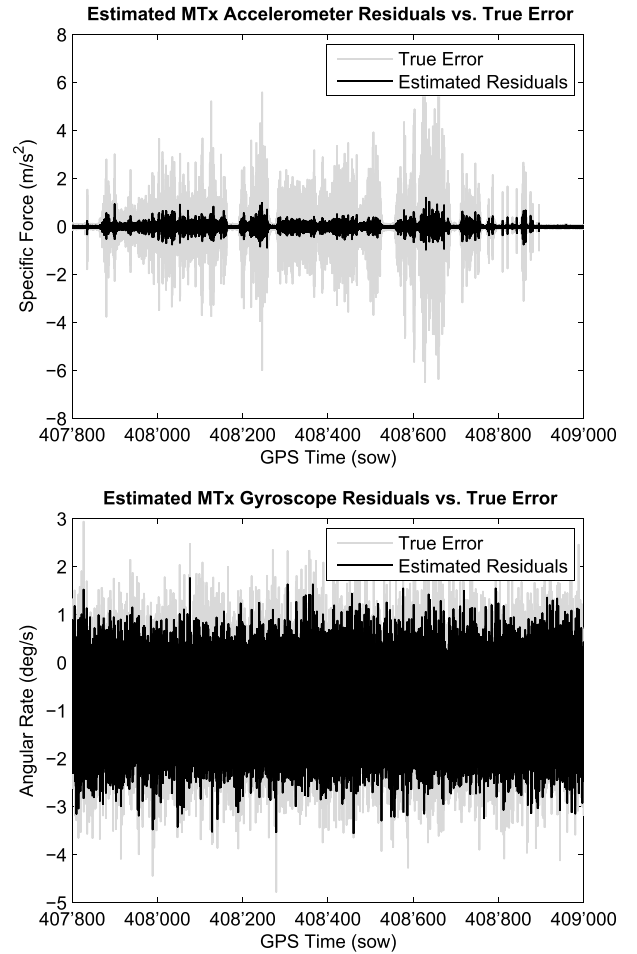


Fig. 8. Adequateness between the residuals estimated from three XSens MTx IMUs, and the true acceleration error (top panel) and angular rate error (bottom panel) with respect to a reference IMU.

signal nonstationary. Therefore, any error model constructed on the static signal will clearly not be representative for the reality when the device is operating in moving conditions.

VII. DEALING WITH DYNAMICS IN NAVIGATION

The results obtained in Sections III and IV prove that calibration results obtained from signals acquired in static conditions may not be sufficient to handle important effects that are present when the platform is moving. In this respect, several options can be considered for taking dynamic-dependent errors into account. If an integrated navigation system is based

TABLE II

ESTIMATED VALUES FOR THE PARAMETERS β_j , $j = 1, \dots, 15$ FOR THE ERROR OF THE GYROSCOPES ON THE x -, y -, OR z -AXIS. THE PRESENTED COEFFICIENTS WERE OBTAINED BY FITTING MODEL (13) ITERATIVELY (STARTING FROM THE FULL MODEL) AND REMOVING AT EACH ITERATION LEAST SIGNIFICANT PARAMETER UNTIL ALL THE PARAMETERS BECAME SIGNIFICANT AT THE 5% CONFIDENCE LEVEL. AT THE BOTTOM, THE R^2 , ADJUSTED R^2 , RESIDUAL VARIANCE (i.e., σ_e^2), AND THE RESULTS (TEST STATISTIC AND p-VALUE) OF F-TEST ARE PRESENTED, WHOSE HYPOTHESES ARE PRESENTED IN (14) FOR EACH MODELS

	Error Gyr. X	Error Gyr. Y	Error Gyr. Z
Angular rate (rad/s)			
ω_x	$2.36 \cdot 10^{-2}$ ($7.87 \cdot 10^{-4}$)***	$-9.89 \cdot 10^{-3}$ ($8.02 \cdot 10^{-4}$)**	$9.6 \cdot 10^{-3}$ ($6.93 \cdot 10^{-4}$)***
ω_y	$6.72 \cdot 10^{-3}$ ($1.64 \cdot 10^{-3}$)***	$3.97 \cdot 10^{-3}$ ($1.65 \cdot 10^{-3}$)*	$-8.16 \cdot 10^{-3}$ ($1.45 \cdot 10^{-3}$)**
ω_z		$-1.67 \cdot 10^{-2}$ ($1.55 \cdot 10^{-3}$)***	$-4.15 \cdot 10^{-3}$ ($1.36 \cdot 10^{-3}$)**
Angular acceleration (rad/s ²)			
$\dot{\omega}_x$	$-5.92 \cdot 10^{-3}$ ($1.51 \cdot 10^{-3}$)***	$-4.65 \cdot 10^{-3}$ ($4.14 \cdot 10^{-4}$)**	$-7.88 \cdot 10^{-3}$ ($3.63 \cdot 10^{-4}$)***
$\dot{\omega}_y$	$3.35 \cdot 10^{-2}$ ($6.62 \cdot 10^{-3}$)***	$-2.64 \cdot 10^{-1}$ ($7.48 \cdot 10^{-3}$)***	$-5.22 \cdot 10^{-2}$ ($6.53 \cdot 10^{-3}$)***
$\dot{\omega}_z$	$-3.52 \cdot 10^{-1}$ ($5.61 \cdot 10^{-3}$)***	$-1.13 \cdot 10^{-1}$ ($5.69 \cdot 10^{-3}$)***	$6.53 \cdot 10^{-2}$ ($4.81 \cdot 10^{-3}$)***
Angular jerk (rad/s ³)			
$\ddot{\omega}_x$	$3.77 \cdot 10^{-1}$ ($2.27 \cdot 10^{-2}$)***	$1.01 \cdot 10^{-1}$ ($2.3 \cdot 10^{-2}$)***	$-2.25 \cdot 10^{-1}$ ($2.02 \cdot 10^{-2}$)***
$\ddot{\omega}_y$	$-6.44 \cdot 10^{-2}$ ($4.42 \cdot 10^{-3}$)***	$1.86 \cdot 10^{-1}$ ($4.77 \cdot 10^{-3}$)***	$4.85 \cdot 10^{-2}$ ($4.17 \cdot 10^{-3}$)***
$\ddot{\omega}_z$	$2.22 \cdot 10^{-1}$ ($4.38 \cdot 10^{-3}$)***	$6.7 \cdot 10^{-2}$ ($4.44 \cdot 10^{-3}$)***	$-2.38 \cdot 10^{-2}$ ($3.85 \cdot 10^{-3}$)***
Acceleration (m/s ²)			
a_x	$2.21 \cdot 10^{-1}$ ($1.55 \cdot 10^{-2}$)***	$1.49 \cdot 10^{-1}$ ($1.57 \cdot 10^{-2}$)***	
a_y	$-2.21 \cdot 10^{-4}$ ($3.51 \cdot 10^{-5}$)***	$-4.22 \cdot 10^{-4}$ ($3.55 \cdot 10^{-5}$)***	$3.61 \cdot 10^{-2}$ ($1.37 \cdot 10^{-2}$)**
a_z	$1.01 \cdot 10^{-4}$ ($2.6 \cdot 10^{-5}$)***	$6.07 \cdot 10^{-4}$ ($5.4 \cdot 10^{-5}$)***	$1.54 \cdot 10^{-3}$ ($4.74 \cdot 10^{-5}$)***
Linear jerk (m/s ³)			
\dot{a}_x	$3.71 \cdot 10^{-3}$ ($8.02 \cdot 10^{-5}$)***	$-6.05 \cdot 10^{-4}$ ($8.17 \cdot 10^{-5}$)***	$-6.52 \cdot 10^{-4}$ ($7.06 \cdot 10^{-5}$)***
\dot{a}_y	$3.54 \cdot 10^{-3}$ ($9.51 \cdot 10^{-5}$)***	$-8.12 \cdot 10^{-3}$ ($9.63 \cdot 10^{-5}$)***	$-6.25 \cdot 10^{-4}$ ($8.04 \cdot 10^{-5}$)***
\dot{a}_z	$5.99 \cdot 10^{-3}$ ($8.63 \cdot 10^{-5}$)***	$-3.05 \cdot 10^{-3}$ ($9.53 \cdot 10^{-5}$)***	$-1.77 \cdot 10^{-4}$ ($8.34 \cdot 10^{-5}$)***
R^2	15.42 %	36.73 %	2.23 %
Adj. R^2	15.42 %	36.73 %	2.22 %
σ_e^2	$1.24 \cdot 10^{-2}$	$1.26 \cdot 10^{-2}$	$6.91 \cdot 10^{-3}$
F-stat	$2.60 \cdot 10^3$	$7.71 \cdot 10^3$	$3.25 \cdot 10^2$
p-value	***	***	***

p-value: 0 *** 0.001 ** 0.01 * 0.05 · 0.1

on higher grade IMUs typically belonging to the tactical- or navigation-grade class, individual gyroscope and accelerometer error models can include terms that depend on quantities

TABLE III

ESTIMATED VALUES FOR THE PARAMETERS β_j , $j = 1, \dots, 15$, FOR THE ERRORS OF THE ACCELEROMETERS ON THE x -, y -, OR z -AXIS. THE PRESENTED COEFFICIENTS WERE OBTAINED BY FITTING MODEL (13) ITERATIVELY (STARTING FROM THE FULL MODEL) AND REMOVING AT EACH ITERATION LEAST SIGNIFICANT PARAMETER UNTIL ALL THE PARAMETERS BECAME SIGNIFICANT AT THE 5% CONFIDENCE LEVEL. AT THE BOTTOM, THE R^2 , ADJUSTED R^2 , RESIDUAL VARIANCE (i.e., σ_e^2), AND THE RESULTS (TEST STATISTIC AND p-VALUE) OF F-TEST ARE PRESENTED, WHOSE HYPOTHESES ARE PRESENTED IN (14) FOR EACH MODELS

	Error Acc. X	Error Acc. Y	Error Acc. Z
Angular rate (rad/s)			
ω_x	$8.86 \cdot 10^{-1}$ ($1.42 \cdot 10^{-2}$)***	1.36 ($1.33 \cdot 10^{-2}$)***	-4.13 ($1.68 \cdot 10^{-2}$)***
ω_y	$-7 \cdot 10^{-2}$ ($2.94 \cdot 10^{-2}$)*	$-7.18 \cdot 10^{-1}$ ($2.74 \cdot 10^{-2}$)***	$-6.13 \cdot 10^{-1}$ ($3.46 \cdot 10^{-2}$)***
ω_z	1.37 ($2.75 \cdot 10^{-2}$)***	$7.77 \cdot 10^{-1}$ ($2.57 \cdot 10^{-2}$)***	-2.37 ($3.23 \cdot 10^{-2}$)***
Angular acceleration (rad/s ²)			
$\dot{\omega}_x$	$6.55 \cdot 10^{-2}$ ($7.34 \cdot 10^{-3}$)***	$8.61 \cdot 10^{-1}$ ($6.86 \cdot 10^{-3}$)***	$-3.59 \cdot 10^{-1}$ ($8.64 \cdot 10^{-3}$)***
$\dot{\omega}_y$	2.77 ($1.33 \cdot 10^{-1}$)***	-7.24 ($1.24 \cdot 10^{-1}$)***	-4.1 ($1.56 \cdot 10^{-1}$)***
$\dot{\omega}_z$	$1.86 \cdot 10^1$ ($1.01 \cdot 10^{-1}$)***	-1.17 ($9.43 \cdot 10^{-2}$)***	$1.28 \cdot 10^1$ ($1.19 \cdot 10^{-1}$)***
Angular jerk (rad/s ³)			
$\ddot{\omega}_x$	-2.75 ($4.08 \cdot 10^{-1}$)***	$-2.58 \cdot 10^1$ ($3.81 \cdot 10^{-1}$)***	$2.12 \cdot 10^1$ ($4.8 \cdot 10^{-1}$)***
$\ddot{\omega}_y$	$8.12 \cdot 10^{-1}$ ($8.46 \cdot 10^{-2}$)***	-4.07 ($7.9 \cdot 10^{-2}$)***	-3.53 ($9.96 \cdot 10^{-2}$)***
$\ddot{\omega}_z$	$2 \cdot 10^{-1}$ ($7.88 \cdot 10^{-2}$)*	3.96 ($7.36 \cdot 10^{-2}$)***	-5.84 ($9.28 \cdot 10^{-2}$)***
Acceleration (m/s ²)			
a_x	$-1.08 \cdot 10^1$ ($2.78 \cdot 10^{-1}$)***	$-2.27 \cdot 10^1$ ($2.59 \cdot 10^{-1}$)***	-5.51 ($3.27 \cdot 10^{-1}$)***
a_y	$-1.85 \cdot 10^{-2}$ ($6.3 \cdot 10^{-4}$)***	$3.24 \cdot 10^{-2}$ ($5.89 \cdot 10^{-4}$)***	$1.22 \cdot 10^{-2}$ ($7.42 \cdot 10^{-4}$)***
a_z	$-2.4 \cdot 10^{-2}$ ($9.58 \cdot 10^{-4}$)***	$-1.33 \cdot 10^{-1}$ ($8.95 \cdot 10^{-4}$)***	$5.55 \cdot 10^{-2}$ ($1.13 \cdot 10^{-3}$)***
Linear jerk (m/s ³)			
\dot{a}_x	$9.47 \cdot 10^{-2}$ ($1.45 \cdot 10^{-3}$)***	$1.4 \cdot 10^{-1}$ ($1.35 \cdot 10^{-3}$)***	$-4.25 \cdot 10^{-1}$ ($1.71 \cdot 10^{-3}$)***
\dot{a}_y	$-1.61 \cdot 10^{-1}$ ($1.71 \cdot 10^{-3}$)***	$1.06 \cdot 10^{-2}$ ($1.6 \cdot 10^{-3}$)***	$1.13 \cdot 10^{-1}$ ($2.01 \cdot 10^{-3}$)***
\dot{a}_z	$1.78 \cdot 10^{-2}$ ($1.69 \cdot 10^{-3}$)***	$2.07 \cdot 10^{-1}$ ($1.58 \cdot 10^{-3}$)***	$-1.01 \cdot 10^{-1}$ ($1.99 \cdot 10^{-3}$)***
R^2	76.65 %	62.30 %	67.65 %
Adj. R^2	76.65 %	62.30 %	67.64 %
σ_e^2	$2.23 \cdot 10^{-1}$	$2.08 \cdot 10^{-1}$	$2.62 \cdot 10^{-1}$
F-stat	$4.36 \cdot 10^4$	$2.20 \cdot 10^4$	$2.78 \cdot 10^4$
p-value	***	***	***

p-value: 0 *** 0.001 ** 0.01 * 0.05 · 0.1

such as angular/linear accelerations and jerk. This approach is the one proposed in [14]. However, when dealing with low-cost MEMS-based devices, an additional acceptable

option (in terms of costs, size, and power consumption) becomes available: the approach of trying to estimate the true (dynamical) errors by introducing redundancy in the navigation system through the use of multiple inertial sensors operating at the same time on the same platform. From these redundant sensors, residuals can be observed, estimated, and included in an adaptive filtering scheme, as recommended in [27].

To which extent this statement is realistic can be deduced from Fig. 8. Fig. 8 shows (in gray) the true *Xsens MTx* accelerometer (top panel) and gyroscope (bottom panel) error signal constructed in Section II. The varying noise level that can be deduced from the plotted estimated residuals is shown as a black line in the respective panels. These estimated residuals were computed from the three *Xsens MTx* units carried on the platform (Fig. 2) by simply computing the residuals around the mean acceleration and angular rate signals. The bottom panel indicates that the gyroscope noise level is fairly well estimated. However, although the accelerometer noise level seems to be under-estimated (top panel), which may be caused by vibration aliasing, the nonmoving and moving conditions can clearly be discriminated from the estimated residuals. The way how to process redundant inertial observations in the mechanization process and the benefits brought in terms of navigation accuracy is, however, beyond the scope of this paper. Nevertheless, information regarding these points can be found in [27]–[29].

VIII. CONCLUSION

We have first described a methodology that allows reliable estimation of spatial and orientation differences between the reference and tested IMUs, even if the latter is of poor quality. Applying this method within a car experiment allowed comparing the observations of low-cost inertial sensors to the reference values separately for each axis. In this way, six time series of errors were created, however, under vehicle dynamic. These underwent the following analysis: first, it was shown that the correlation between the observed errors and the vehicle dynamics is statistically significant. Then, a model structure was created, and the model parameters were estimated via the GMWM methodology, the principles of which were briefly reviewed. When comparing this model with that obtained under static conditions, we conclude that although the model structure did not change, the model parameters are significantly different. In future, we plan to investigate the relevance of the obtained model-parameter value (e.g., as used within the Kalman Filter) on the quality of the integrated navigation.

REFERENCES

- [1] W. T. Fong, S. Ong, and A. Y. C. Nee, “Methods for in-field user calibration of an inertial measurement unit without external equipment,” *Meas. Sci. Technol.*, vol. 19, no. 8, p. 085202, 2008.
- [2] D. Titterton and J. Weston, *Strapdown Inertial Navigation Technology*. Stevenage, U.K.: Peregrinus, 1997.
- [3] IEEE Standard Specification Format Guide and Test Procedure for Coriolis Vibratory Gyros, IEEE Standard 1431, 2004.
- [4] J. K. Bekkeng, “Calibration of a novel MEMS inertial reference unit,” *IEEE Trans. Instrum. Meas.*, vol. 58, no. 6, pp. 1967–1974, Jun. 2009.
- [5] A. Chatfield, *Fundamentals of High Accuracy Inertial Navigation*. Washington, DC, USA: AIAA, 2004.
- [6] D. W. Allan, “Statistics of atomic frequency standards,” *Proc. IEEE*, vol. 54, no. 2, pp. 221–230, Feb. 1966.
- [7] N. El-Sheimy, H. Hou, and X. Niu, “Analysis and modeling of inertial sensors using Allan variance,” *IEEE Trans. Instrum. Meas.*, vol. 57, no. 1, pp. 140–149, Jan. 2008.
- [8] S. Guerrier, J. Skaloud, Y. Stebler, and M.-P. Victoria-Feser, “Wavelet-variance-based estimation for composite stochastic processes,” *J. Amer. Statist. Assoc.*, vol. 108, no. 503, pp. 1021–1030, 2013.
- [9] S. Guerrier, “Two essays in statistics: A prediction divergence criterion for model selection & wavelet variance based estimation of latent time series models,” Ph.D. dissertation, Dept. Res. Center Statist., Univ. Geneva, Geneva, Switzerland, 2013.
- [10] Y. Stebler, S. Guerrier, J. Skaloud, and M.-P. Victoria-Feser, “Generalized method of wavelet moments for inertial navigation filter design,” *IEEE Trans. Aerosp. Electron. Syst.*, vol. 50, no. 3, pp. 2269–2283, Jul. 2014.
- [11] I. Bar-Itzhack and R. Harman, “Implicit and explicit spacecraft gyro calibration,” in *Proc. AIAA GNC Conf. Exhibit*, 2004, pp. 1–17, paper AIAA 2004-5343.
- [12] M. E. Pittelkau, “Kalman filtering for spacecraft system alignment calibration,” *J. Guid. Control Dyn.*, vol. 24, no. 6, pp. 1187–1195, Nov./Dec. 2001.
- [13] X. Niu, C. Goodall, S. Nassar, and N. El-Sheimy, “An efficient method for evaluating the performance of MEMS IMUs,” in *Proc. IEEE/ION Position Location Navigat. Symp. (PLANS)*, San Diego, CA, USA, Apr. 2006, pp. 766–771.
- [14] M. Wis and I. Colomina, “Dynamic dependency of inertial sensor errors and its application to INS/GNSS navigation,” in *Proc. NAVITEC Congr.*, Noordwijk, The Netherlands, Dec. 2010, pp. 1–7.
- [15] Y. Stebler, S. Guerrier, J. Skaloud, R. Molinari, and M.-P. Victoria-Feser, “Study of MEMS-based inertial sensors operating in dynamic conditions,” in *Proc. IEEE/ION Position, Location Navigat. Symp.*, May 2014, pp. 1227–1231.
- [16] B. Scherzinger, “Inertial navigator error models for large heading uncertainty,” in *Proc. IEEE/ION Position Location Navigat. Symp.*, Apr. 1996, pp. 477–484.
- [17] A. Wägli, “Trajectory determination and analysis in sports by satellite and inertial navigation,” Ph.D. dissertation, Ecole polytechnique fédérale de Lausanne, Lausanne, Switzerland, 2009.
- [18] J. A. Farrell, *Aided Navigation: GPS With High Rate Sensors*. New York, NY, USA: McGraw-Hill, 2008.
- [19] “Department of defense world geodetic system 1984: Its definition and relationships with local geodetic systems,” Nat. Imagery Mapping Agency, Tech. Rep., 1997.
- [20] Y. Stebler, S. Guerrier, J. Skaloud, and M. Victoria-Feser, “A framework for inertial sensor calibration using complex stochastic error models,” in *Proc. IEEE/ION Position, Location Navigat. Symp.*, Apr. 2012, pp. 849–861.
- [21] D. B. Percival and A. T. Walden, *Wavelet Methods for Time Series Analysis* (Cambridge Series in Statistical and Probabilistic Mathematics). New York, NY, USA: Cambridge Univ. Press, 2000.
- [22] N. F. Zhang, “Allan variance of time series models for measurement data,” *Metrologia*, vol. 45, no. 5, p. 549, 2008.
- [23] C. Gourieroux, A. Monfort, and E. Renault, “Indirect inference,” *J. Appl. Econ.*, vol. 8, no. S1, pp. S85–S118, Dec. 1993.
- [24] R. G. Brown and P. Y. C. Hwang, *Introduction to Random Signals and Applied Kalman Filtering*, 2nd ed. New York, NY, USA: Wiley, 1997.
- [25] A. E. Bryson, *Applied Linear Optimal Control: Examples and Algorithms*. Cambridge, U.K.: Cambridge Univ. Press, 2002.
- [26] Z. Xing, “Over-bounding integrated INS/GNSS output errors,” Ph.D. dissertation, Dept. Aerosp. Eng. Mech., Univ. Minnesota, Minneapolis, MN, USA, Oct. 2010.
- [27] A. Waegli, J. Skaloud, S. Guerrier, M. Parés, and I. Colomina, “Noise reduction and estimation in multiple micro-electro-mechanical inertial systems,” *Meas. Sci. Technol.*, vol. 21, no. 6, pp. 065201-1–065201-11, 2010.
- [28] Y. Stebler, S. Guerrier, J. Skaloud, and M.-P. Victoria-Feser, “Improving modeling of MEMS-IMUs operating in GNSS-denied conditions,” in *Proc. 24th Int. Tech. Meeting Satellite Division Inst. Navigat. (ION GNSS)*, Sep. 2011, pp. 1–10.
- [29] S. Guerrier, “Improving accuracy with multiple sensors: Study of redundant MEMS-IMU/GPS configurations,” in *Proc. 22nd Int. Tech. Meeting Satellite Division Inst. Navigat.*, 2009, pp. 3114–3121.



Yannick Stebler received the M.Sc. degree in navigation techniques and geomatics engineering from the École Polytechnique Fédérale de Lausanne (EPFL), Lausanne, Switzerland, and the Ph.D. degree from the Robotics and Manufacturing Systems School, EPFL.



Stéphane Guerrier received the M.Sc. degree in geomatics engineering from the École Polytechnique Fédérale de Lausanne (EPFL), Lausanne, Switzerland, in 2008, with a focus on the integration of redundant microelectromechanical systems-inertial measurement units with global positioning system, and the Ph.D. degree in statistics from the University of Geneva, Geneva, Switzerland, in 2013, with a focus on signal processing for navigation applications.

He is currently an Assistant Professor with the Department of Statistics, University of Illinois at Urbana-Champaign, Champaign, IL, USA. His current research interests include model selection and the estimation of stochastic processes.



Jan Skaloud received the Ph.D. and M.Sc. degrees in geomatics engineering from the University of Calgary, Calgary, AB, Canada, and the Dipl.-Ing. degree from Czech Technical University in Prague, Prague, Czech Republic.

He is currently a Lecturer and Senior Scientist with the École Polytechnique Fédérale de Lausanne, Lausanne, Switzerland.

Dr. Skaloud was the Chair of the International Society for Photogrammetry and Remote Sensing Working Group on Integrated Systems for Mobile Mapping from 2008 to 2012. In 2009, he was recognized by the *GPS World* journal as one of the world's 50 most influential scientists in the field of satellite navigation.